Floating bridge response under combined ship collision, wind and wave loads

Zihao Wang, Yanyan Sha & Jasna Bogunović Jakobsen

Published online: 18 Apr 2023.

Submit your article to this journal ↗

View related articles ↗

View Crossmark data ↗

Taylor & Francis
Taylor & Francis Group

Floating bridge response under combined ship collision, wind and wave loads

Zihao Wang ⬡, Yanyan Sha ⬡ and Jasna Bogunović Jakobsen ⬡

Department of Mechanical and Structural Engineering and Materials Science, University of Stavanger, Stavanger, Norway

ABSTRACT

Floating bridges over navigable fjords with exposed substructures are at risk of accidental ship collisions. Other hazards such as extreme wind and wave loads are also critical for floating bridges. This study investigates the global dynamic responses of a floating bridge subjected to different combinations of ship collision, wind and wave loads. A numerical model of a floating bridge is developed using OrcaFlex. The ship-bridge interaction is modelled by defining a constraint element attached to the striking ship. The stiffness of the constraint is described by a nonlinear force-displacement curve. The full turbulent wind field is generated using TurbSim, and the bridge buffeting response is calculated in time domain based on the linear quasi-steady theory. The wind-bridge interaction is accounted for by considering the relative angle of attack and the relative wind velocity at each time step. The bridge responses under individual hazards are compared with those considering multi-hazards.

1. Introduction

Bridges have a significant role in the development of transportation networks. Across very deep and wide waterways, the construction of traditional bridges with fixed supports is not feasible due to the costs and technical challenges. The concept of floating bridges supported by pontoons can be an economical solution based on the current technology. In the past few decades, several large floating bridges have been designed and constructed worldwide (Watanabe 2003). The Norwegian Public Roads Administration has initiated a coastal highway project E39 in western Norway, to establish a ferry-free connection between Trondheim and Kristiansand. Floating bridges are being considered as relevant structural concepts to cross the 1.6–5 km wide and 400–1300 m deep fjords. Design and construction of floating bridges crossing navigable fjords are challenging due to their structural flexibility and complex loading environment. A wide range of potential natural or man-made hazards, such as hurricanes, earthquakes, tsunami and ship collisions, might pose significant threats to floating bridges. These hazards may potentially lead to excessive structural responses and damages which consequently result in traffic disruptions, environmental damage, economic losses, and human injuries and casualties.

Floating bridges are constantly subjected to environmental loads during service life, including wind and wave loads. Strong wind and large waves can induce extreme load effects on bridges. During severe weather conditions such as hurricanes, typhoons or tsunami, the induced wind or wave loads acting on bridges are significantly higher than what is normally expected. It is vital to consider the potential hazards caused by increased loads and ensure that the bridges are designed to withstand these extreme conditions. Bridge response to wind loads needs to be considered, both regarding the effects of turbulence as well as possible aerodynamic instabilities. Wave-induced forces can cause relative movement of pontoons, which may lead to fatigue on the bridge structures. When resonant responses are excited by the combination of wind and wave loads,

excessive bridge motion may be induced (Cheng et al. 2018a). Meanwhile, floating bridges crossing navigable waterways are at risk of accidental ship collisions, possibly caused by human errors, technical errors such as steering and engine failures, or terrorist attacks. The high kinetic energy of colliding ships imposes a threat to bridge structures if accidental collisions occur. If bridge pontoons struck by ships undergo excessive damage, potential loss of water-tightness may lead to flooding and consequently cause the collapse of the entire bridge superstructure (Sha and Amdahl 2019).

In engineering practice, potential hazards on bridge structures are usually treated as individual and independent phenomena. For instance, bridge structures are commonly designed for either wind loads or ship collision loads separately in the horizontal directions. Many research endeavours could be found in the literature to investigate the bridge performance subjected to individual hazards. Previous research efforts have been made in assessing bridge response against wind loads (Mikkelsen and Jakobsen 2017; Wang et al. 2018; Cheynet et al. 2022; Costa et al. 2022), wave loads (Sha et al. 2018; Cheng et al. 2018b; Viuff et al. 2020; Cui et al. 2022; Fenerci et al. 2022) and ship collisions (Fan et al. 2011; Moe et al. 2017; Sha and Amdahl 2017; Gholipour et al. 2018). Even though the occurrence probability of several hazards arising simultaneously or sequentially is relatively low, an unanticipated combination of multiple hazards can cause disastrous consequences to bridge structures and their surrounding communities (Bruneau et al. 2017). Multi-hazard events imposed on bridge structures are more frequent nowadays (Li et al. 2012; Banerjee et al. 2019). The vulnerability of large bridge structures increases significantly when multiple hazards occur within a short period, or when the unrepaired damage from one hazard is followed by another.

One of the pioneer studies on multi-hazard analysis was conducted by Rackwitz and Flessler (1978), who focused on determining the occurrence probability of several time-variant stochastic actions based on the first-order probability methods. The combined

CONTACT Zihao Wang ✉ zihao.wang@uis.no ▣ Department of Mechanical and Structural Engineering and Materials Science, University of Stavanger, Stavanger 4021, Norway

effect of different loading conditions was evaluated assuming the loads or actions can be modelled by independent, stationary random sequences. Gill and Malamud (2016) proposed a multi-hazard risk assessment framework to integrate hazard interactions (triggering, catalysis/impedance and increased probability). It was found that by adopting the single-hazard approach to assess hazard potential, the risk of other spatially relevant hazards would be underestimated, while the multi-hazard methodology can contribute to an improved theoretical and practical understanding of the risks of hazards. Argyroudis et al. (2019) further examined the vulnerability of bridge structures against multi-hazards by proposing a risk assessment framework integrating multi-hazard fragility functions. It was discovered that the predictions of structural behaviour, vulnerability and failure modes were more realistic when the hazard interactions were taken into consideration in numerical analyses. Oppong et al. (2020) investigated the vulnerability of fixed foundation river-crossing bridges under barge collisions followed by hurricane events. By comparing the structural responses of both intact and damaged bridges, they suggested that the residual damage from collision accidents can significantly increase bridge vulnerability to subsequent hurricane-induced wave loads.

However, to date, there is no available research addressing the structural behaviour and responses of floating bridges under combined wind, wave and ship collision loads. According to Eurocode (2006) and N400 (Statens Vegvesen 2015), bridge structures must be designed to meet the performance requirements after any structural damage to avoid malfunction and failure. Therefore, response analyses of floating bridges with respect to multi-hazards are deemed necessary to be performed in the design phase. This study aims to investigate the multi-hazard effects on the structural responses of a floating bridge over Bjørnafjord through time-domain simulations. The focus is on the global dynamic response of the bridge structure subjected to combined wind, wave and ship collision loads. The floating bridge response against multi-hazards is first compared with the bridge response under individual hazards. Subsequently, different ship collision parameters such as collision instant, ship mass, collision energy and collision location are investigated in multi-hazard analyses.

The multi-hazard assessment framework developed in this study can be useful in the design and analysis of floating bridge structures.

2. Finite element modelling

Bjørnafjord is located south of Bergen and is approximately 5 km wide and 550 m deep. The Bjørnafjord-crossing bridge concept is an end-anchored curved floating bridge supported by pontoons with a supplementary side-mooring system. The key geometrical and structural properties are presented in this section (Statens Vegvesen 2019a, 2019c). Figure 1 illustrates the studied bridge concept for the Bjørnafjord-crossing floating bridge.

The bridge structure has a total arc length of 5530 m and consists of three parts: a cable-stayed part, a high floating bridge, and a low floating bridge, as shown in Figure 1. The southern end of the bridge starts with a straight cable-stayed part, supported by a 200 m tall concrete tower. There is a free span that yields a navigable channel with a width of 270 m. The pontoon-supported floating part is curved in the horizontal plane with a 5000 m radius of curvature. The end abutments, concrete tower, and columns above pontoons are labelled as A1 to A41, accordingly. The floating bridge that spans between A3 and A41 rests on 38 pontoons with a distance of 125 m. The bridge height decreases gradually from the south to the north and the height of pontoon columns ranges from 10.5 m to 45.6 m. Three groups of side-mooring systems connected to the pontoons at A13, A20, and A27 provide additional lateral and vertical stiffness to the bridge.

2.1. Modelling of bridge structure

A numerical model of the floating bridge is developed in OrcaFlex (Orcina 2022a), as illustrated in Figure 2. Structural components including the bridge deck, tower, piers, stay cables, mooring lines, columns and pontoons are modelled. There are different cross-sectional characteristics for the bridge deck along the bridge alignment (Statens Vegvesen 2019f). The floating bridge part is made of steel and each floating span has three types of sections: one locally strengthened
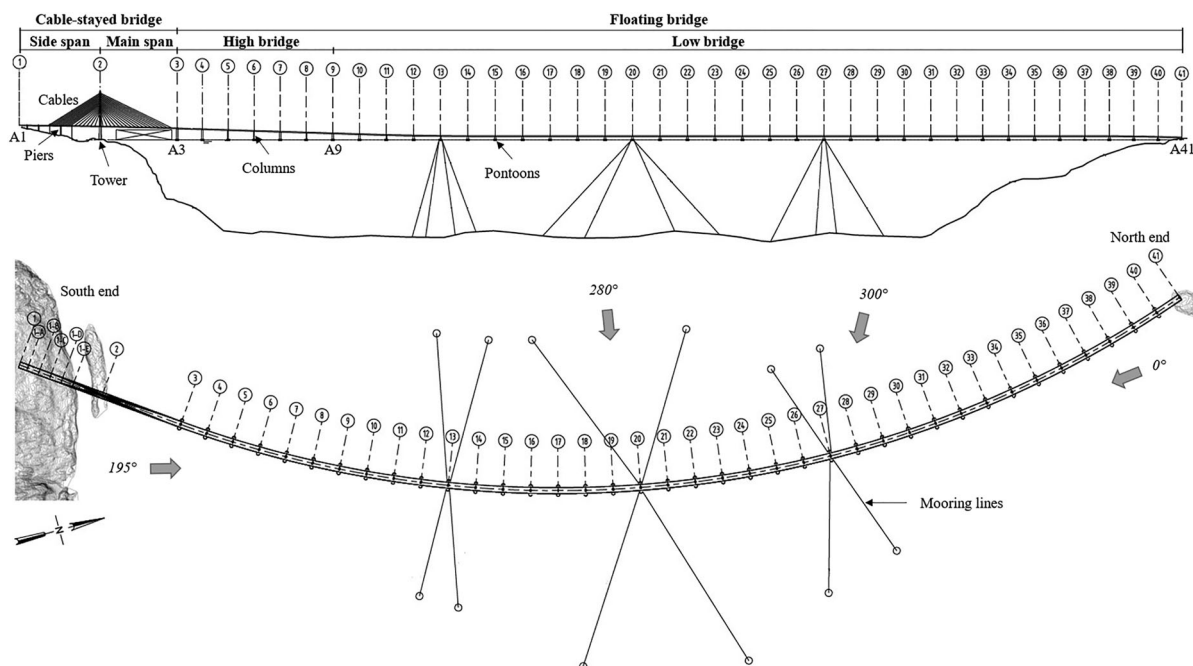

Figure 1. Bjørnafjord floating bridge concept, modified from Statens Vegvesen (2019b).
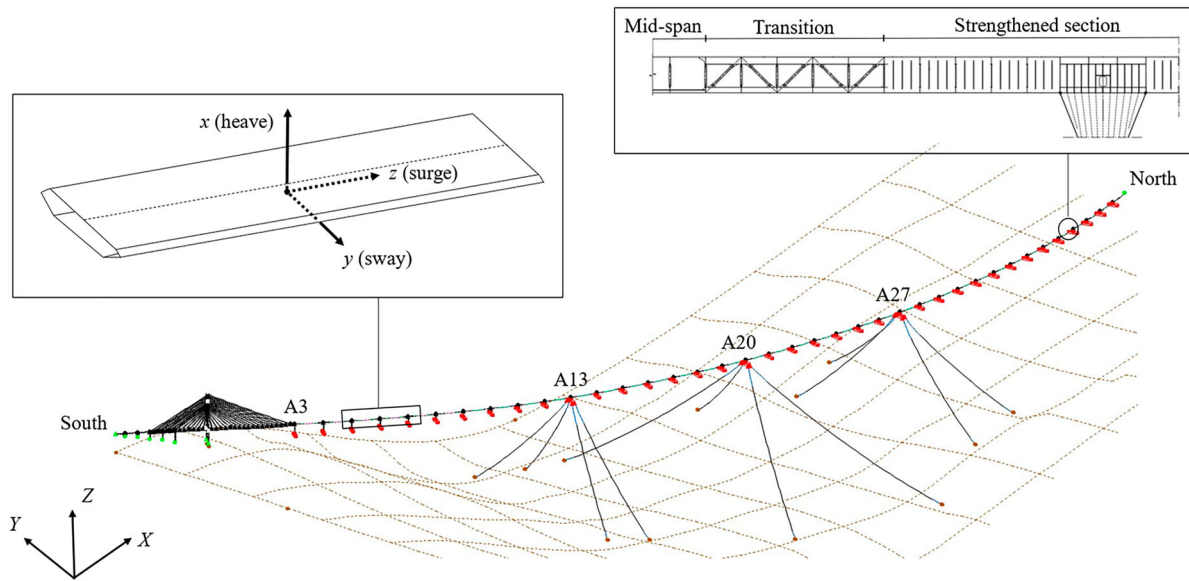
Figure 2. Finite element model of the floating bridge in OrcaFlex. (This figure is available in colour online.)

Table 1. Cross-sectional properties of the high floating bridge part and low floating bridge part.

Cross-section	Mass [ton/m]	Bending stiffness [kN·m^2]		Axial stiffness [kN]	Torsional stiffness [kN·m^2]
		x	y		
S_H	19.0	2.64×10^{10}	1.01×10^{9}	4.06×10^{8}	9.08×10^{8}
T_H	19.0	2.17×10^{10}	8.48×10^{8}	3.26×10^{8}	7.72×10^{8}
M_H	19.0	1.96×10^{10}	7.63×10^{8}	2.95×10^{8}	7.24×10^{8}
S_L	19.0	2.37×10^{10}	9.37×10^{8}	3.76×10^{8}	8.51×10^{8}
T_L	19.0	2.17×10^{10}	8.48×10^{8}	3.26×10^{8}	7.72×10^{8}
M_L	19.0	1.85×10^{10}	7.16×10^{8}	2.81×10^{8}	6.61×10^{8}

Note: S = strengthened section; T = transition section; M = mid-span section; H = high floating bridge; L = low floating bridge.

section above pontoon columns, one slimmer section at midspan, and another transition section in between. The corresponding structural properties of each cross-section can be found in Table 1.

The bridge deck is fixed at the south and north ends in all degrees of freedom, and the bridge tower is fixed at two tower legs. A group of 72 stay cables connects the bridge deck to the tower. The pretension force levels of the stay cables range from 2300 to 5250 kN (Statens Vegvesen 2019c). All the pontoon columns have rigid connections with the bridge deck and pontoons. The bridge piers in the back span of the cable-stayed part are connected rigidly to the bridge deck and the ground.

OrcaFlex line objects are used for modelling the bridge deck, columns, the tower, stay cables, and mooring lines. Each line object is divided into a series of straight massless line segments modelling the axial, bending and torsional properties, and other properties such as mass, weight and buoyancy are lumped to the nodes. For stay cables and mooring lines, compression and torsion are not included in element modelling. The bridge deck line is assumed to follow the neutral axis of the real deck cross-section, and the eccentricity of different sections is not accounted for. The influence of this assumption on the global bridge response is negligible. The mooring lines are composed of a bottom chain, a middle chain, and a top chain with different properties (Statens Vegvesen 2019g). The pretension forces in the mooring lines and stay cables are adjusted iteratively to reach the target designed values. The structural damping is considered by the Rayleigh damping for all bridge components which are modelled as lines. Pontoons are modelled as rigid vessel objects with both hydrostatic and hydrodynamic properties. The masses of the

pontoons are ballasted to achieve a vertical equilibrium between buoyancy and self-weight.

2.2. Hydrostatic and hydrodynamic modelling of pontoons

The pontoons are made of steel and consist of outer shell plates and inner stiffeners and bulkheads. Both the conventional (without additional mooring lines) pontoons and the moored pontoons are 53 m long and 14.9 m wide. The design draft is 5 m for conventional pontoons, as illustrated in Figure 3. For moored pontoons, the immersed depth is increased to 7.5 m for a larger buoyancy to compensate for the vertical forces from the mooring lines. The buoyancy of the pontoons is determined by the centre of buoyancy and the displaced volume. The main hydrostatic properties including mass, moment of inertia and hydrostatic stiffness are presented in Table 2 for both the conventional and moored pontoons. The centre of gravity and metacentre for each pontoon can be referred to the technical report from Statens Vegvesen (2019a). Pontoons at A13, A20 and A27 are moored to the seabed with four mooring lines for each location. The pretension forces of twelve mooring lines range from 1980 to 2590 kN. The mechanical and hydrodynamic properties of different components of mooring lines are shown in Table 3.

Frequency-dependent added mass, potential damping, and response amplitude operators (RAOs) are important parameters for wave loads in dynamic analyses. They are calculated in OrcaWave (Orcina 2022b) based on the linear potential theory. Figure 3 illustrates the panel model used for the conventional pontoons, as well as the six degrees of freedom considered in the radiation problem. The average mesh size of the model is approximately
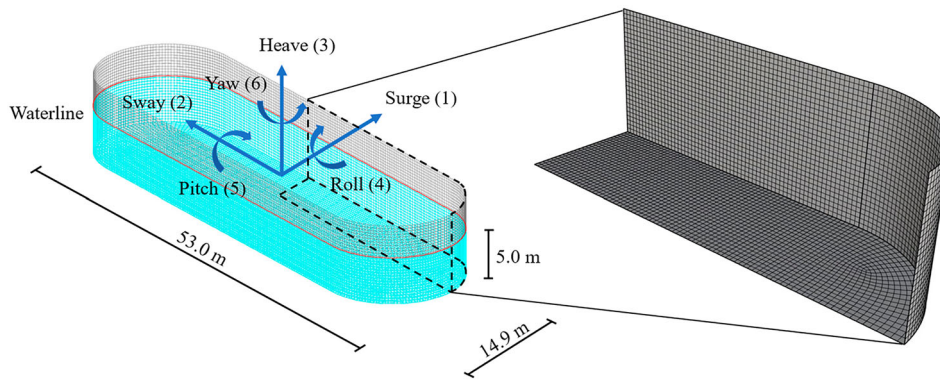
Figure 3. Panel model used for the conventional pontoons. (This figure is available in colour online.)

Table 2. Structural and hydrostatic properties of pontoons.

			Conventional pontoons	Moored pontoons
Mass	M	[ton]	1361	3256
Draft	D	[m]	5.0	7.5
Freeboard	B	[m]	3.5	3.5
Displaced volume	V	[m³]	3709.3	5564.0
Moment of inertia	I_{xx}	[ton·m²]	2.95×10^5	6.60×10^5
	I_{yy}	[ton·m²]	4.55×10^4	1.68×10^5
	I_{zz}	[ton·m²]	2.89×10^5	5.97×10^5
Hydrostatic stiffness	C_{33}	[kN/m]	7.46×10^3	7.46×10^3
	C_{44}	[kN·m/rad]	1.56×10^6	1.04×10^6
	C_{55}	[kN·m/rad]	1.29×10^5	8.62×10^4

0.3 m. The added mass and potential damping of pontoons in sway, heave, and roll are presented in Figure 4. Both the conventional and moored pontoons have similar added mass in heave and roll. However, the moored pontoons have significantly larger added mass in sway. There is a minor difference in the potential damping in heave for both types of pontoons. The potential damping of moored pontoons is higher in sway and lower in roll compared with the conventional pontoons.

2.3. Eigenvalue analysis

Eigenvalue analysis is conducted to determine the dynamic properties of the floating bridge model. The bridge is very flexible and has eigenmodes with long periods. The periods of the first hundred eigenmodes vary from about one minute to four seconds. Six selected eigenmodes are presented in Table 4. The first 5 modes are mainly dominated by bending in the horizontal plane and rotation about the longitudinal bridge axis, and have periods from 56.361 to 15.889 s. Notably, there is a large number of local modes dominated by mooring lines from mode No. 6, which has a period of 13.538 s. Starting from mode No. 64 with a period of 5.127 s, vertical bending modes with local mooring modes are dominating. Higher eigenmodes may be critical if resonant motions in

the vertical direction are excited. The results from eigenvalue analysis imply that the first few vibration modes with longer periods will be excited by the wind loads and ship collisions. Regarding the wave effects, the fifth mode with an eigen-period of 15.889 s is in the range of the frequencies of swell. Higher eigenmodes with periods between 4 and 5 s are dominated by vertical bending due to the heave motion of pontoons. These modes are in the critical regime of wind-wave, as well as for wind loads due to smaller-scale/high frequency turbulence. It is notable that the hydrodynamic and aerodynamic frequency-dependent contributions to mass, stiffness and damping are not accounted for in the eigenvalue analysis due to the limitations of the software, i.e. only the 'dry modes' are analysed here. When comparing the eigenmodes of the current bridge model to the reference report (Statens Vegvesen 2019c), the modal shapes and the corresponding frequencies of the first five modes show good agreement with those in the reference report considering the frequency-dependent mass, stiffness and damping. For higher modes with higher frequencies, the mode shapes are however slightly different due to the small variations in mooring line pretensions. During time domain simulations, all frequency-dependent mass, damping and stiffness are included in dynamic analyses.

3. Modelling of load conditions

The wind and wave load conditions considered in this study are for 100-year return period. Different combinations of wind, wave and ship collision loads are investigated in different load cases. The design environmental conditions for the Bjørnafjord, including wind, wind-wave, and swell are obtained from the MetOcean report from Statens Vegvesen (2018). The three-dimensional turbulent wind field is generated using TurbSim (Jonkman and Kilcher 2012), developed by the US National Renewable Energy Laboratory (NREL). The stochastic wave field is generated in OrcaFlex based on wave spectrum and direction spectrum. The key elements in the modelling of hazards considered in this study are presented in Figure 5.

Table 3. Mechanical and hydrodynamic properties of mooring line components.

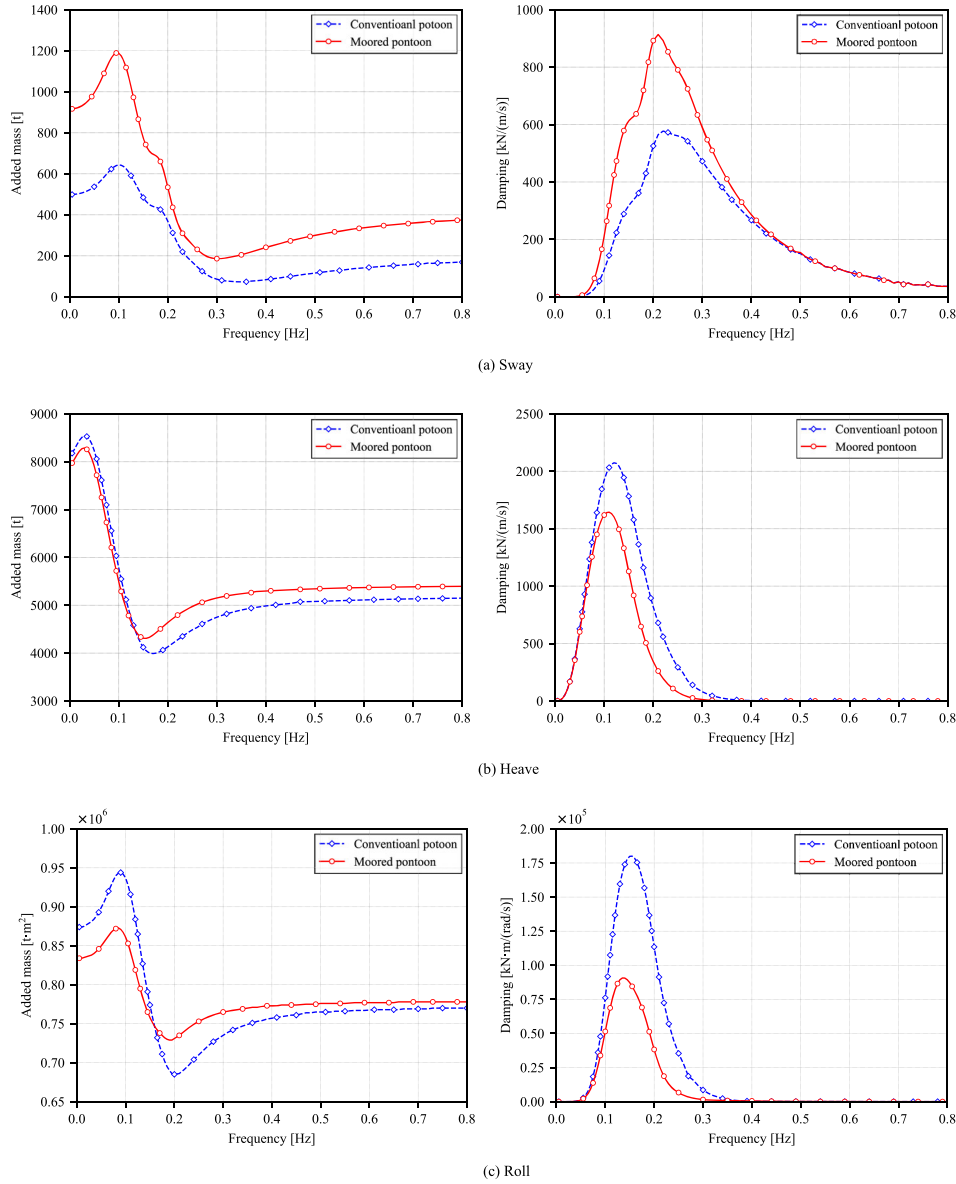|			Top chain	Middle wire	Bottom chain
Weight in water		[kg/m]	376.0	65.3	376.0
Axial stiffness		[kN]	1.73×10^6	1.45×10^6	1.73×10^6
Drag coefficient	Longitudinal direction	[–]	1.15	0.10	1.15
	Transverse direction	[–]	2.4	1.2	2.4
Added mass coefficient	Longitudinal direction	[–]	0	0	0
	Transverse direction	[–]	1.0	1.0	1.0

Figure 4. Added mass and potential damping in (a) sway; (b) heave; and (c) roll for the conventional and moored pontoons. (This figure is available in colour online.)

3.1. Modelling of wind loads

The stochastic wind field is modelled including a steady wind component $\bar{U}(z)$ and a fluctuating part $u(t)$, $v(t)$ and $w(t)$ in the along-wind, lateral and vertical directions, respectively. The 10-min mean wind speed at a reference height of 10 m is chosen as 25.2 m/s (Statens Vegvesen 2019d). The vertical wind profile of the mean wind speed follows the logarithmic profile with a surface roughness z_0 of 0.01 m, as defined in the Eurocode (2007). The wind velocities are simulated in a rectangular grid with 265 points distributed horizontally with a spacing of 20 m, and 23 vertically distributed points with a 10 m distance. The 3-D turbulent wind field is generated based on the IEC Kaimal spectrum $S_k(f)$, defined by Equation (1):

$$S_k(f) = \frac{4\sigma_k^2 L_k/\bar{U}_{mid}}{(1 + 6fL_k/\bar{U}_{mid})^{5/3}}; \quad k = u, v, w \quad (1)$$

where f is the wind frequency, σ_k is the standard deviation for k component, L_k represents the integral scale parameter, and $\bar{U}_{mid}$ is the mean wind velocity at the middle height in the wind simulation grid.
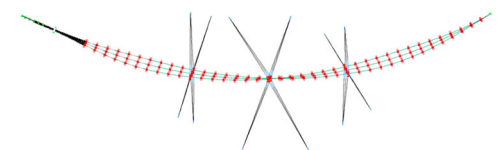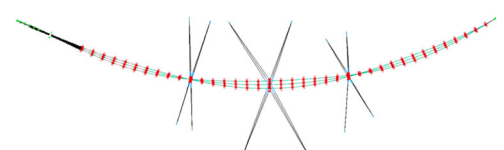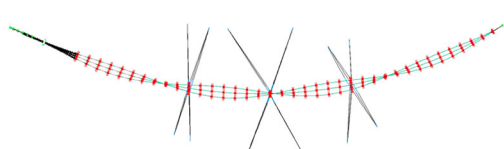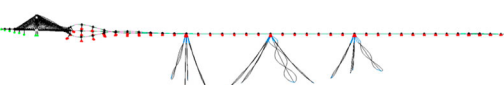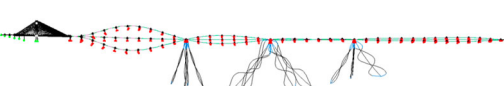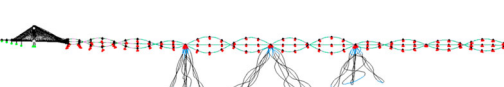
The turbulence model of the fluctuating wind components is selected as the Normal Turbulence Model (NTM) with turbulence Class C. The coherence model (IEC 61400-1 2005) for the three turbulence components is given by Equation (2):

$$Coh_k = exp\left[-a_k\sqrt{\left(\frac{fs}{\bar{U}_{mid}}\right)^2 + (b_k s)^2}\right]; \quad k = u, v, w \quad (2)$$

where Coh_k represents the coherence between two points, a_k is the coherence decrement parameter, b_k is the offset parameter, and s is the spatial distance between two different locations.

The bridge buffeting response under wind loads is calculated in the time-domain based on the linear quasi-steady theory. The load is modelled in terms of three components: the drag force in the along-wind direction F_D, the lift force in the cross-wind direction F_L, and the moment about the bridge longitudinal axis M, as illustrated in Figure 6. The linearised functions for the time-varying

Table 4. Selected eigenmodes information of the floating bridge model.

Mode	Period [s]	Mode shape	Dominating motion
1	56.361		Horizontal bending and rotation about longitudinal axis
2	43.508		Horizontal bending and rotation about longitudinal axis
3	30.804		Horizontal bending and rotation about longitudinal axis
74	4.580		Vertical bending and local mooring mode
76	4.520		Vertical bending and local mooring mode
84	4.454		Vertical bending and local mooring mode
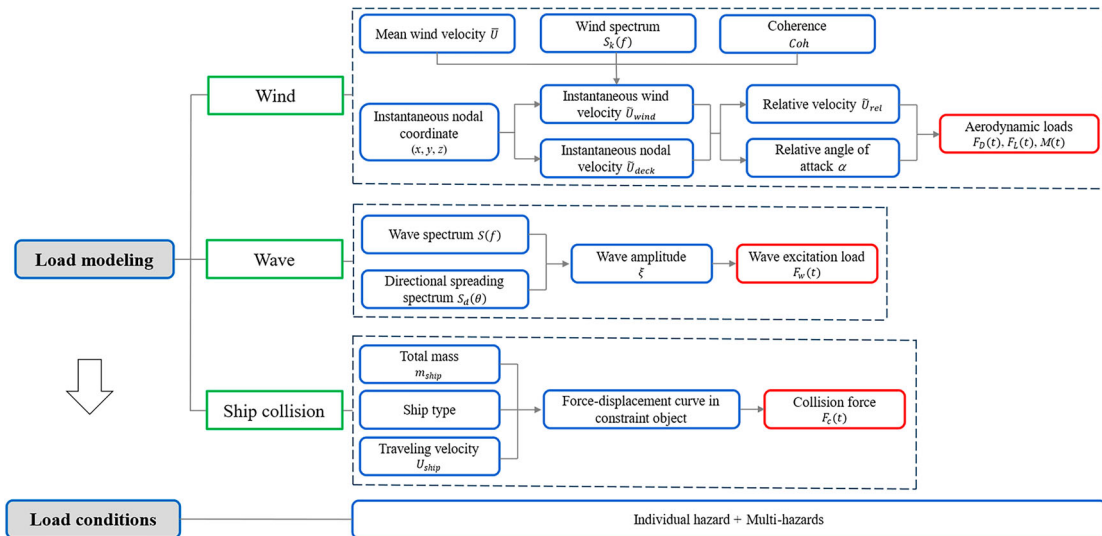
Figure 5. Key elements in the modelling of different hazards and considered load conditions. (This figure is available in colour online.)

forces are given in Equations (3)–(5):

$$F_D = \frac{1}{2}\rho\tilde{U}_{rel}^2 HL(\bar{C}_D + \alpha C_D') \tag{3}$$

$$F_L = \frac{1}{2}\rho\tilde{U}_{rel}^2 BL(\bar{C}_L + \alpha C_L') \tag{4}$$

$$M = \frac{1}{2}\rho\tilde{U}_{rel}^2 B^2 L(\bar{C}_M + \alpha C_M') \tag{5}$$
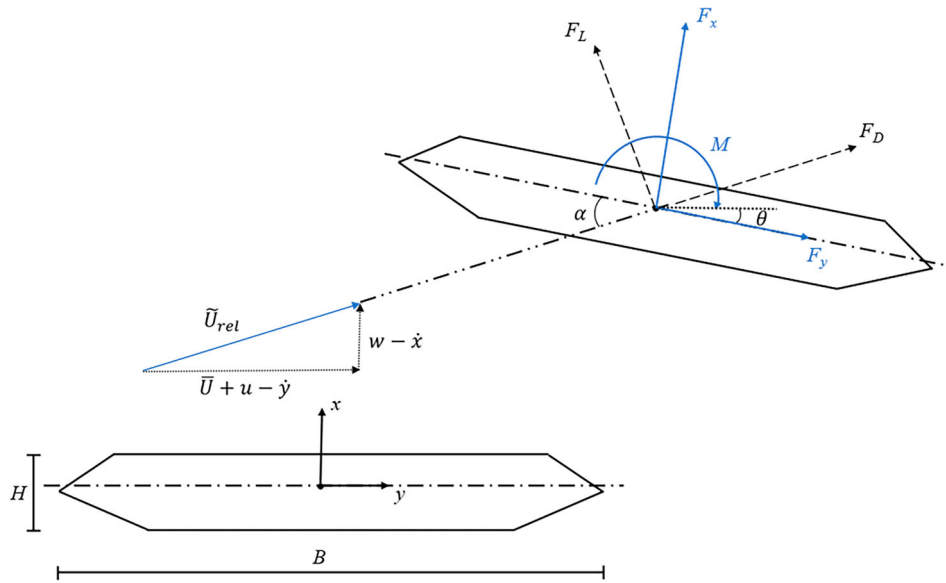
Figure 6. Relative instantaneous velocity, angle of attack, and aerodynamic forces. (This figure is available in colour online.)

where ρ is the air density, $\tilde{U}_{rel}$ represents the instantaneous wind velocity relative to the bridge deck, H is the cross-sectional height, B is the cross-sectional width, L is the distance between two structural nodes where wind loads are applied, α is the instantaneous relative angle of attack. $\bar{C}_D$, $\bar{C}_L$ and $\bar{C}_M$ represent the drag, lift, and moment coefficients when α equals to zero, and C'_D, C'_L and C'_M represent the aerodynamic coefficient gradients, respectively.

The time series of turbulent wind velocities is simulated in Turb-Sim based on the mean wind speed, wind gust spectrum and coherence function. External Python functions are developed to transform the time-varying wind velocities to dynamic wind loads acting on bridge deck nodes in the local coordinate system. Instantaneous coordinates of the bridge deck nodes are obtained in each time step and the wind velocities at these nodes are linearly interpolated from the wind velocity data of the nearest grid points. Turbulence simulated in the vertical grid plane is applied to the nodes along the arch bridge axis by considering the relevant time delay due to the curvature of bridge, i.e. assuming 'frozen turbulence'. It should be noted that the wind velocity component along the bridge axis is neglected in this study for simplification. As shown in Figure 6, the instantaneous wind velocity field relative to the moving structure is considered, as well as the relative instantaneous angle of attack, i.e. both the aerodynamic damping and stiffness are accounted for. The adopted mean force coefficients at zero angle of attack, as well as the associated gradients with respect to the angle of attack, are presented in Table 5.

It should be noted that, in the present phase of the analysis, the aerodynamic loads are only considered on the bridge deck, as the major contributor to the global response under the wind loads. The wind-exposed area of the bridge columns above pontoons is about 10% of the bridge deck in the along-wind direction.

3.2. Modelling of wave loads

The wave conditions in the Bjørnafjord can be modelled as short-crested irregular waves, including both local wind-generated waves and swell from the ocean (Statens Vegvesen 2018). The short-term sea state is considered stationary, and the wave field is assumed to be homogeneous along the bridge span in the present analyses. The first-order wave load considered on the pontoons is calculated using the transfer functions as introduced in Section 2.2. The JONSWAP spectrum $S(f)$ and wave spreading spectrum $S_d(\theta)$ are applied to generate the stochastic wave field. The wave spectra for wind-generated wave and swell used in this study are illustrated in Figure 7. The JONSWAP spectrum (DNV 2018) is given by Equation (6):

$$S(f) = \frac{\alpha g^2}{16\pi^4} f^{-5} \exp\left[-\frac{5}{4}\left(\frac{f}{f_m}\right)^{-4}\right] \gamma^{\exp\left[-\frac{1}{2\sigma^2}\left(\frac{f}{f_m}-1\right)^2\right]} \quad (6)$$

where α is the spectral energy parameter, g is the gravitational acceleration, f_m represents the spectral peak frequency, γ is the peak enhancement factor, and σ is the spectral width parameter.

The wave directions are distributed by applying the equal energy strategy, which gives a *cos-n* type narrow spreading around the main wave direction. The distribution of wave direction is considered by applying the directional wave spectra and the total spectrum $S(f, \theta)$ can be expressed as:

$$\begin{aligned} S(f,\theta) &= S(f)S_d(\theta) \\ &= S(f)\frac{\Gamma(1+0.5n)}{\sqrt{\pi}\Gamma(0.5+0.5n)} cos^n(\theta-\theta_c) \\ &\quad \text{for} -\frac{\pi}{2} \leq \theta - \theta_c \leq \frac{\pi}{2} \end{aligned} \quad (7)$$

where n is the spreading exponent, θ is the wave direction, and θ_c represents the principal wave direction.

The input parameters for the wave spectra and directional spectra are selected based on the design basis (Statens Vegvesen 2019c). After the total wave spectrum is applied for generating a short-term sea state, the wave elevation can be interpreted as a function of the significant wave height H_s, the peak spectrum period T_p, the principal wave direction θ_c, and the random seed to generate the phase angle ε_{nm}. All pontoons are subjected to the same wave conditions. In time-domain analysis, OrcaFlex solves the equations of motion containing frequency-dependent added mass and potential

Table 5. Aerodynamic coefficients for the bridge deck.

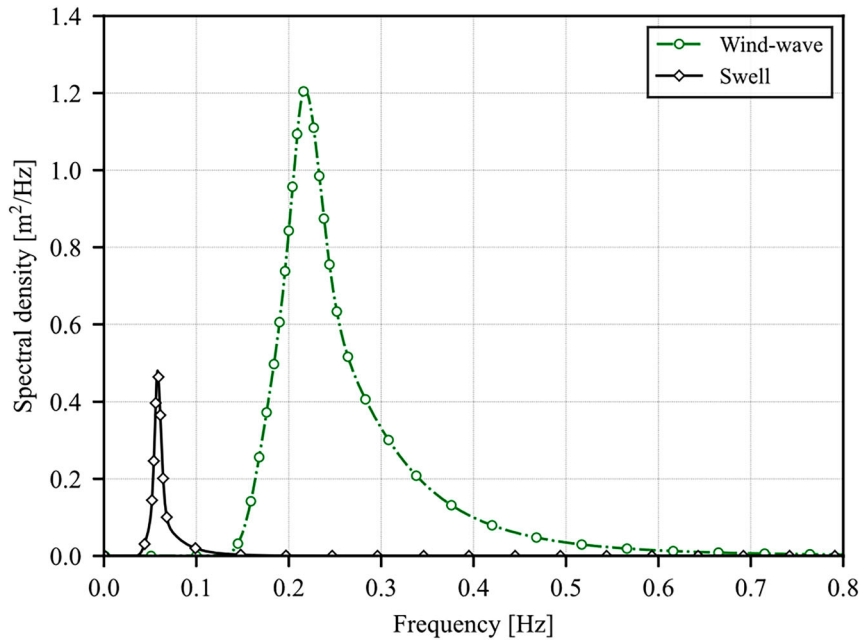| Aerodynamic coefficients	$\bar{C}_D$	C'_D	$\bar{C}_L$	C'_L	$\bar{C}_M$	C'_M
Value	0.949	−2.330	−0.378	3.591	−0.019	1.165

Figure 7. Wave spectra for wind-wave and swell, with parameters given in Table 6. (This figure is available in colour online.)

Table 6. Applied wave data and spectral parameters of JONSWAP spectra.

	Wind-wave	Swell
Significant wave height H_s [m]	1.40	0.34
Spectrum peak period T_p [s]	4.60	17.25
Number of wave directions	15	15
Spreading exponent n	8	8
Peak enhancement factor γ	1.8	5.0

damping by adopting the method proposed by Cummins (1962):

$$\sum_{k=1}^{6} \left\{ [M_{sk} + A_{sk}^{\infty}]\ddot{x}_k^{(1)} + D_{sk}\dot{x}_k^{(1)} + [K_{sk} + C_{sk}]x_k^{(1)} \right.$$
$$\left. + \int_{\tau=0}^{\infty} IRF(\tau)\dot{x}_k^{(1)}(t-\tau)d\tau \right\} = F_w^{(1)}(t) \qquad (8)$$

$$IRF(\tau) = c(\tau) \int_{f=0}^{\infty} 4B(f)\cos(2\pi ft)df \qquad (9)$$

where M_{sk} is the structural mass, A_{sk}^{∞} is the added mass at infinite frequency, D_{sk} represents the structural damping, K_{sk} represents the structural stiffness, C_{sk} represents the hydrostatic stiffness, IRF is the impulse response function, $F_w^{(1)}$ represents the first-order wave excitation load, $\ddot{x}_k^{(1)}$, $\dot{x}_k^{(1)}$ and $x_k^{(1)}$ represent the time-dependent acceleration, velocity, and displacement, respectively. $B(f)$ is the potential damping at frequency f. $c(\tau)$ is the cutoff scaling function, τ is the time shift, and the convolution integral term considers the time memory effect.

3.3. Modelling of ship collision

Due to the limitations on the commonly available computational resources for finite element simulations, the analyses of long floating bridges against ship collisions are simplified into two parts: local structural damage assessment and global bridge response analysis (Sha et al. 2019). A local model of impacted bridge section is usually defined with fixed boundary conditions to investigate the local structural damage during a collision event. Since the energy dissipation from the global bridge motion is not included, the local deformation and damage might be overestimated. Global analysis is commonly performed with two objectives: (1) to determine the global motion and other global responses including internal forces and moments, and (2) to obtain the energy dissipations in local and global responses. This study focuses on the global dynamic response of the floating bridge under multi-hazard scenarios, i.e. the external dynamics between the striking ship and the bridge is the emphasis in the simulations. It should be noted that by using the simplified ship-bridge system, the residual damage of both the ship and the struck pontoon can not be well captured. Only head-on collisions are considered in the current analyses.

The interaction between the striking ship and the struck pontoon is modelled by a constraint element attached to the ship bow. The constraint has only one translational degree of freedom along the collision direction. Its translational stiffness is defined by a nonlinear force-displacement curve obtained from local analysis for two representative ship bow-pontoon collision scenarios (Sha and Amdahl 2019; Jin et al. 2021), as shown in Figure 8. The nonlinear constraint stiffness is treated as hysteretic to model the inelastic stiffness effect depending upon the past motion.

The added mass of the ship in the surge direction is taken as 10% of the ship mass (Eurocode 2006). The ship motions in yaw and roll and the ship wave-generated waves are not considered. Ship motions and ship wave-generated waves might cause additional loads on pontoons. These influences could be further discussed in future investigations. The ship motion is initiated by an external force acting at the centre of gravity. The external force is removed right before the ship contacts the pontoon when the desired ship velocity is achieved. After the collision process between the striking ship and the struck pontoon is completed, the ship is set to drift away freely and will not interact with the bridge structure again. It is notable that the ship can collide with pontoons with different incidence angles and secondary contact might occur. However, this will have negligible influence on the maximum response at the collision location.
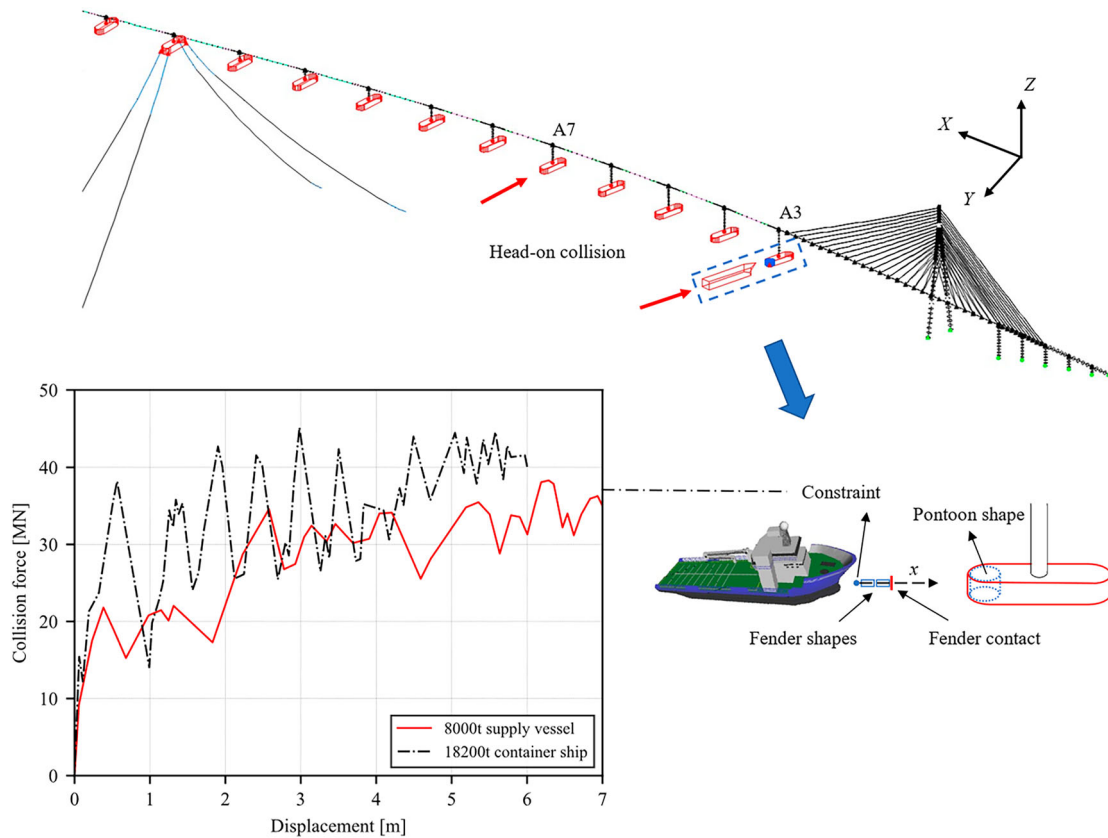
Figure 8. Ship collision modelling and different force-displacement curves for the modelled constraint object. (This figure is available in colour online.)

4. Load cases in time-domain simulation

With the above-described load input from wind, wave, and ship collision, time-domain simulation is conducted to investigate the global structural response of the considered bridge concept under various loading conditions. Due to the computational challenge on the interactions between the simulation and external functions, the duration of each simulation is chosen as 10 mins with a time step of 0.01 s for this study. The simulation for each load case lasts 780 s and the first 180 s is the ramping phase which is omitted in the dynamic analysis results to opt-out the transient effect. In

principle, the simulation period and the ramping phase can be extended for practical design.

The structural responses of the Bjørnafjord floating bridge under the individual wind and wave conditions were investigated by Statens Vegvesen (2019d). Different loading conditions are considered in this study to investigate the effects of different combinations of multi-hazards, as listed in Table 7. A reference load case with only self-weight and buoyancy of the bridge structure is marked as LC 0.1. The load cases LC 1.1, LC 1.2, and LC 1.3 are single hazard scenarios with wind load, wave

Table 7. Load cases for time-domain simulation.

	Wind		Wind-wave / Swell			Ship collision				
	$\bar{U}$ [m/s]	Dir. [°]	H_s [m]	T_p [s]	Dir. [°]	Location	Energy [MJ]	Mass [t]	Velocity [m/s]	Instant
LC 0.1	Load case with permanent load only									
LC 1.1	25.2	280	–	–	–	–	–	–	–	–
LC 1.2	–	–	1.40 / 0.34	4.60 / 17.25	195 / 300	–	–	–	–	–
LC 1.3	–	–	–	–	–	A3	110.0	8000	5.00	–
LC 1.4	25.2	280	1.40 / 0.34	4.60 / 17.25	195 / 300	–	–	–	–	–
LC 2.1										I(−)
LC 2.2	25.2	280	1.40 / 0.34	4.60 / 17.25	195 / 300	A3	110.0	8000	5.00	I(+)
LC 2.3										I(0)
LC 3.1							70.4	8000	4.00	
LC 3.2	25.2	280	1.40 / 0.34	4.60 / 17.25	195 / 300	A3	158.4	8000	6.00	I(0)
LC 3.3							70.4	18200	2.65	
LC 3.4							160.0	18200	4.00	
LC 4.1										I(−)
LC 4.2	25.2	280	1.40 / 0.34	4.60 / 17.25	195 / 300	A7	110.0	8000	5.00	I(+)
LC 4.3										I(0)

Note: '–' represents no input value for the corresponding hazard parameter.
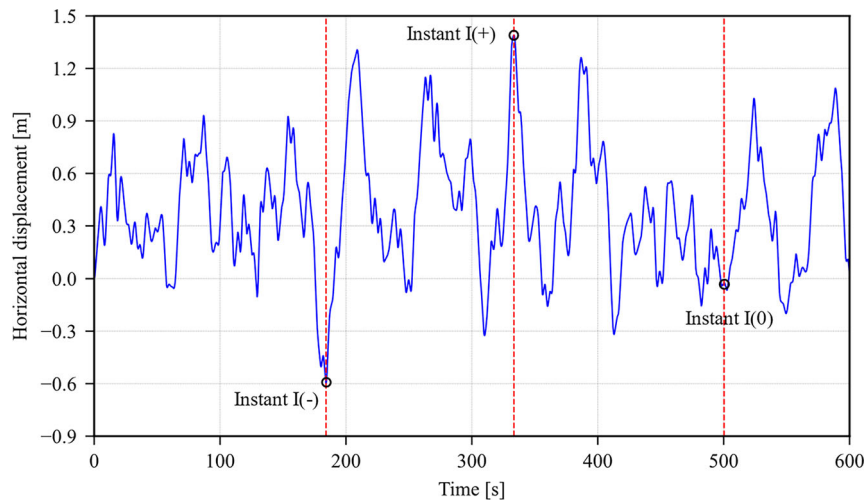
Figure 9. Time history of the horizontal displacement at A3 under combined wind and wave loads (LC 1.4). (This figure is available in colour online.)
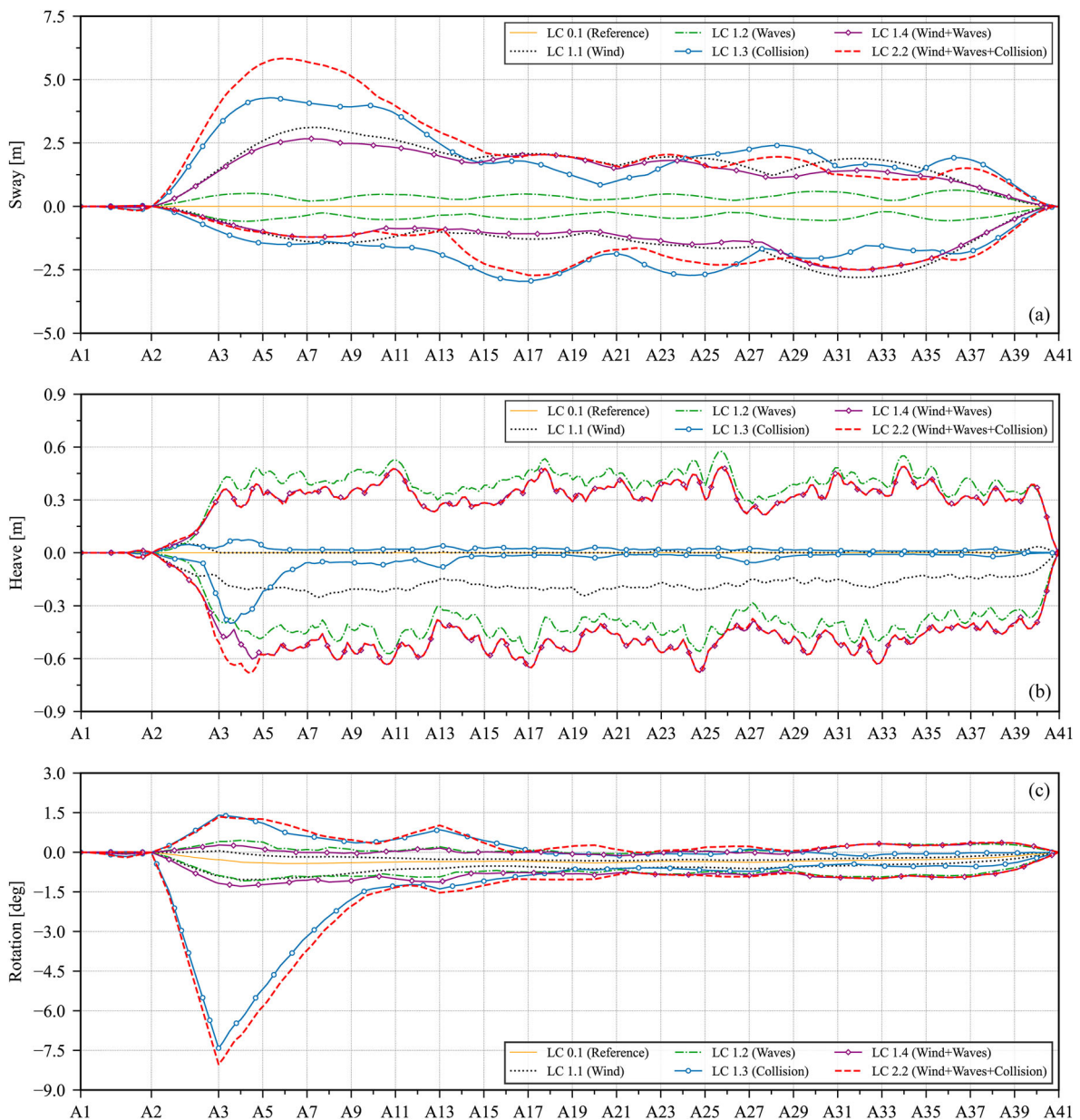

Figure 10. Maximum dynamic motion of the bridge deck under single-hazard and multi-hazard load cases (a) sway – horizontal displacement; (b) heave – vertical displacement; (c) rotation about the longitudinal axis. (This figure is available in colour online.)

load, and ship collision load, respectively. The ship collision location is first assumed to be at pontoon A3, which is the closest pontoon to the navigable channel in the high bridge part. The scenario with combined wind and wave loads is labelled as LC 1.4. For multi-hazard scenarios, the cases considering combined wind, wave, and ship collision loads are named LC 2.1 to LC 4.3.

In engineering practice, the ship candidates and their velocities in bridge design against collision accidents are analysed by risk assessment. Over the last two decades, the experienced ship size and impact velocity have been increased in historical collision accidents (Kvitrud 2011). The chosen striking ship in the case study is selected as an 8000-t supply vessel (with 10% added mass) and the collision velocity is assumed as 5 m/s, which leads to a collision energy of 110 MJ (Statens Vegvesen 2019h).

Three different instants are considered in the load cases to account for the variation in ship collision instant, as illustrated in Figure 9. Instant I(-) represents the time step when the struck pontoon has the largest sway motion in the opposite direction of the collision under combined wind and wave loads (LC 1.4). The instant when the pontoon has the maximum wind and wave-induced horizontal displacement along the collision direction is labelled as Instant I(+). Instant I(0) is a representative time step when the horizontal displacement of the pontoon is approximately zero. The pontoon velocities in the sway direction are approximately zero for all three instants.

The variations in the collision energy, ship mass, and striking velocity are considered in LCs 3.1–3.4. Furthermore, LCs 4.1–4.3 study the representative multi-hazard conditions at different collision locations. It should be noted that the ship orientation in each analysis is adjusted according to the

simultaneous pontoon position at the exact collision starting time to ensure a head-on collision. A more detailed definition of all the parameters of considered load cases is presented in Table 7. The directions of the applied wind and wave loads can be referred to Figure 1.

5. Dynamic response of the floating bridge

The global dynamic behaviour of the floating bridge in terms of structural motions and internal forces and moments under various load cases is presented in this section. This study focuses on the maximum responses in both positive and negative bridge axes in the time-domain simulations. The horizontal and vertical displacements, rotation about the bridge longitudinal axis, horizontal and vertical accelerations, horizontal shear forces, and bending moments about both strong and weak axes of the bridge deck are analysed. The effect of multi-hazards on the structural behaviour of the considered floating bridge is addressed first. Then, the variations in the bridge dynamic responses due to different ship collision parameters are investigated in multi-hazard scenarios.

5.1. Comparison between single- and multi-hazard conditions

The maximum bridge deck displacements and rotations are plotted along the bridge longitudinal axis in Figure 10. It should be noted that the maximum values do not occur simultaneously at each bridge location but at different instants throughout the entire time history. As shown in Figure 10(a), the load cases considering only wind (LC 1.1), and combined wind and waves (LC 1.4) give
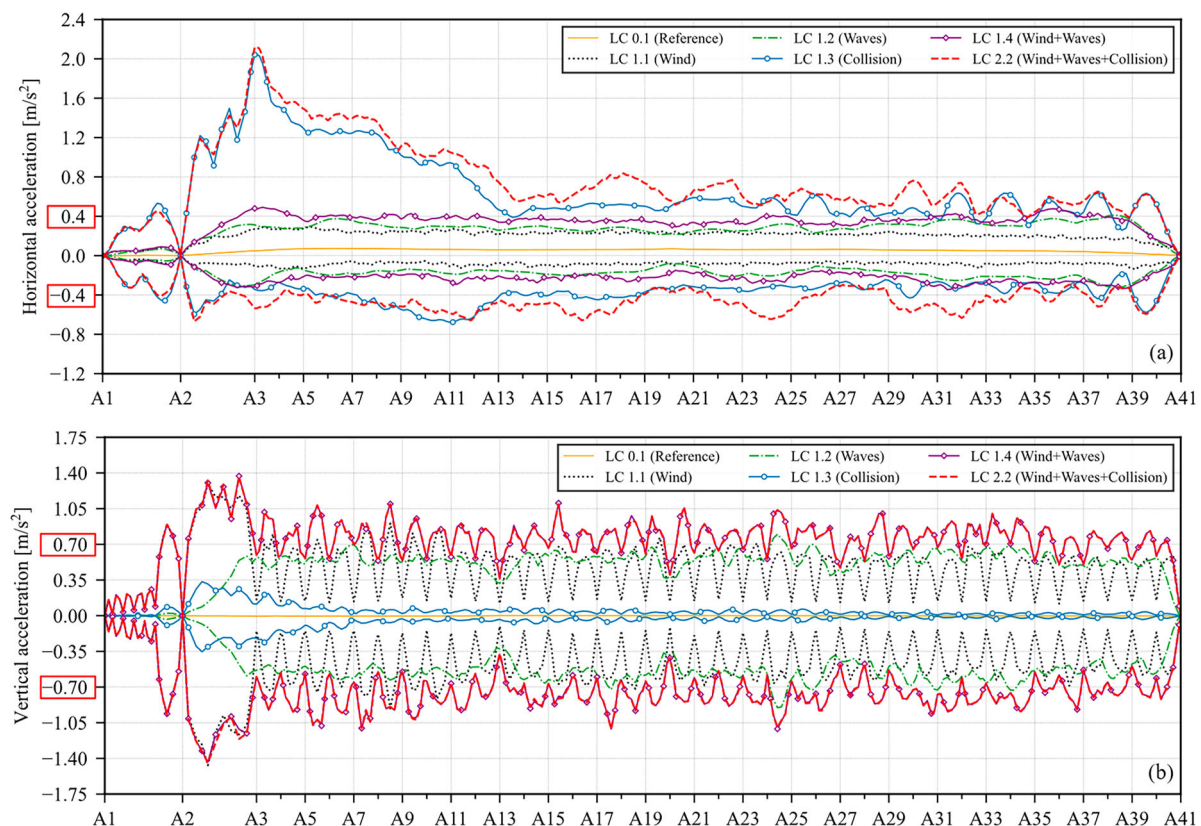
Figure 11. Maximum accelerations of the bridge deck under single-hazard and multi-hazard load cases (a) horizontal acceleration; (b) vertical acceleration. (This figure is available in colour online.)
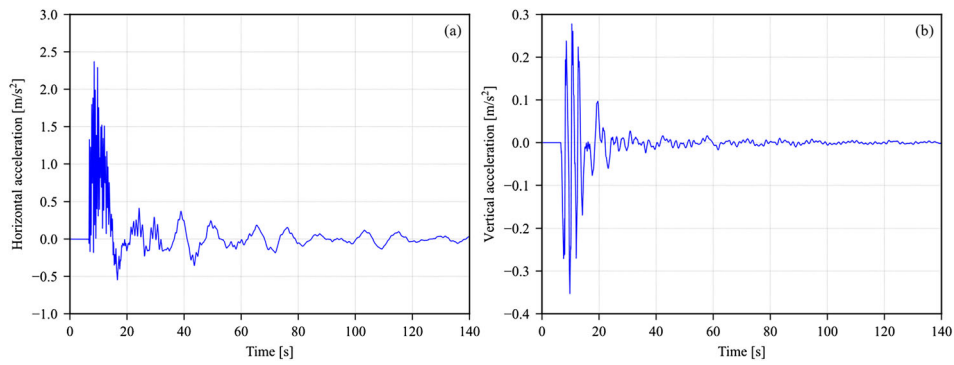
Figure 12. Time history of A3 accelerations in individual ship collision load case. The time origin is the starting time of the excitation force for the ship (a) horizontal acceleration time history; (b) vertical acceleration time history. (This figure is available in colour online.)
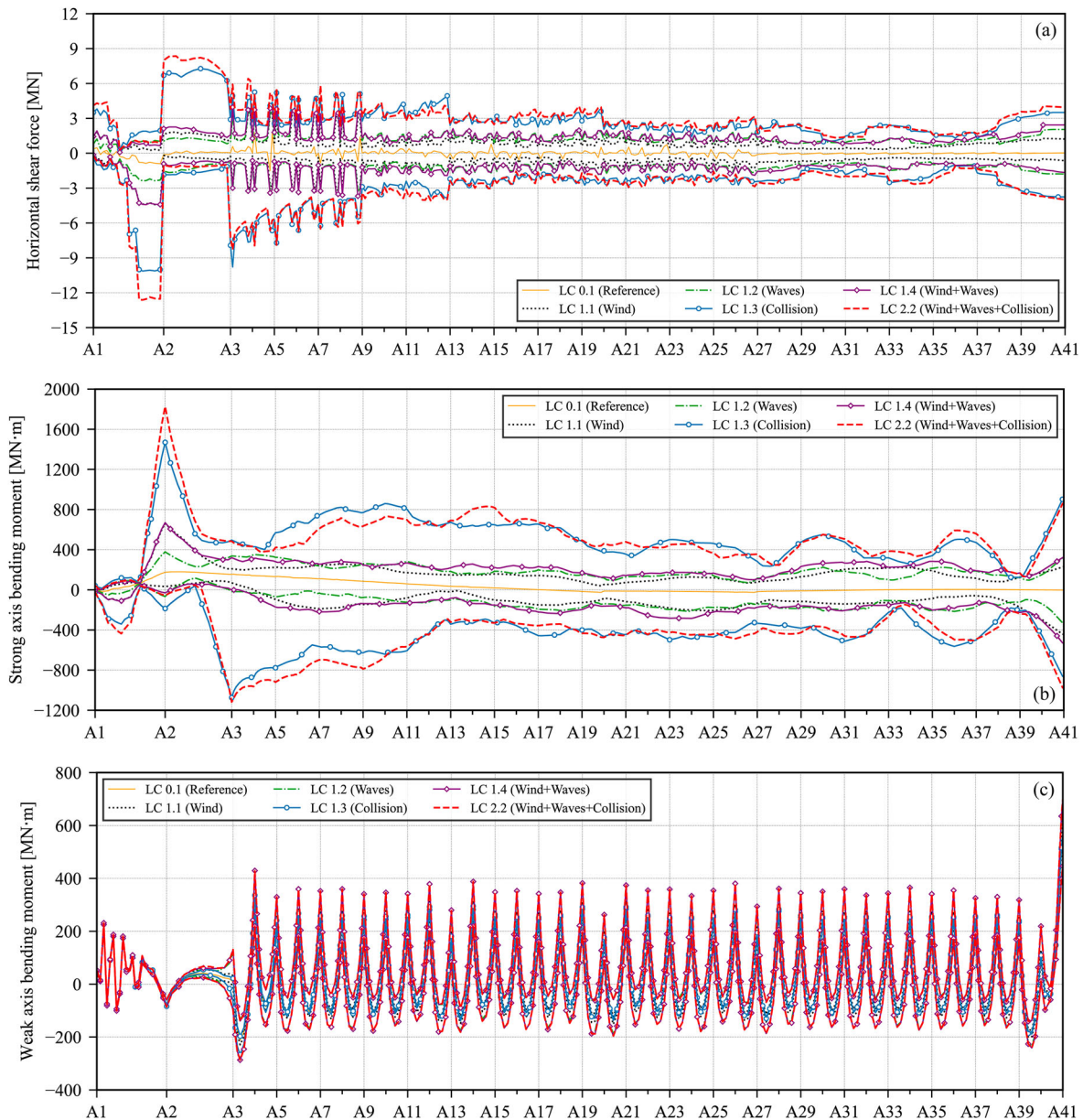

Figure 13. Maximum force and moment of the bridge deck under single-hazard and multi-hazard load cases (a) horizontal shear force; (b) strong axis bending moment; (c) weak axis bending moment. (This figure is available in colour online.)

similar maximum horizontal displacements of approximately 3.1 and 2.7 m, respectively. The maximum sway displacement in the pure ship collision case (LC 1.3) shows about 4.3 m at A5. As can be observed, the sway motion envelopes under combined wind and wave conditions are asymmetric about the middle of the bridge. Due to the arch shape of the floating bridge and the presence of a mooring system, the maximum sway motion on the north side is not as large as on the south side for the pure collision and multi-hazard load condition (LC 2.2). The horizontal displacements in LCs 1.1, 1.4 and 2.2 reach their peaks in the vicinity of A7. The reason is that the bridge is quite flexible and A7 is located at the middle of two bridge constraints, namely the tower at A2 and the mooring group at A13. Compared with other single-hazard load cases, the multi-hazard load case yields the largest horizontal displacement of 5.8 m. The envelopes for the sway motion under wind load are similar to a superposition of the first few eigenmodes of the floating bridge, in agreement with the fact that most of the wind energy is dissipated at low frequencies. Besides, the envelopes

for the response under indivudual wave loads (LC 1.2) suggest that eigenmodes with higher frequencies are excited by high-frequency wind-wave and swell.

Figure 10(b) illustrates the maximum vertical displacements of the bridge deck. As expected, the turbulent wind load contributes much less to the heave than the wave load. The contribution of ship collision to the maximum vertical displacement in multi-hazard analysis primarily influences A4 and its adjacent locations, since the collision load has a short duration and the effect is quickly damped out.

Similarly, as can be observed in Figure 10(c), the analyses with pure ship collision and multi-hazard conditions yield large rotations of the bridge deck at the collision location A3, which are about 7.4 and 8.0 degrees, respectively. At the instant when ship collision is completed, the rotation reaches its maximum at the collision location, resulting in a large wind relative angle of attack. This may lead to large instantaneous aerodynamic forces and moments acting on the bridge deck.
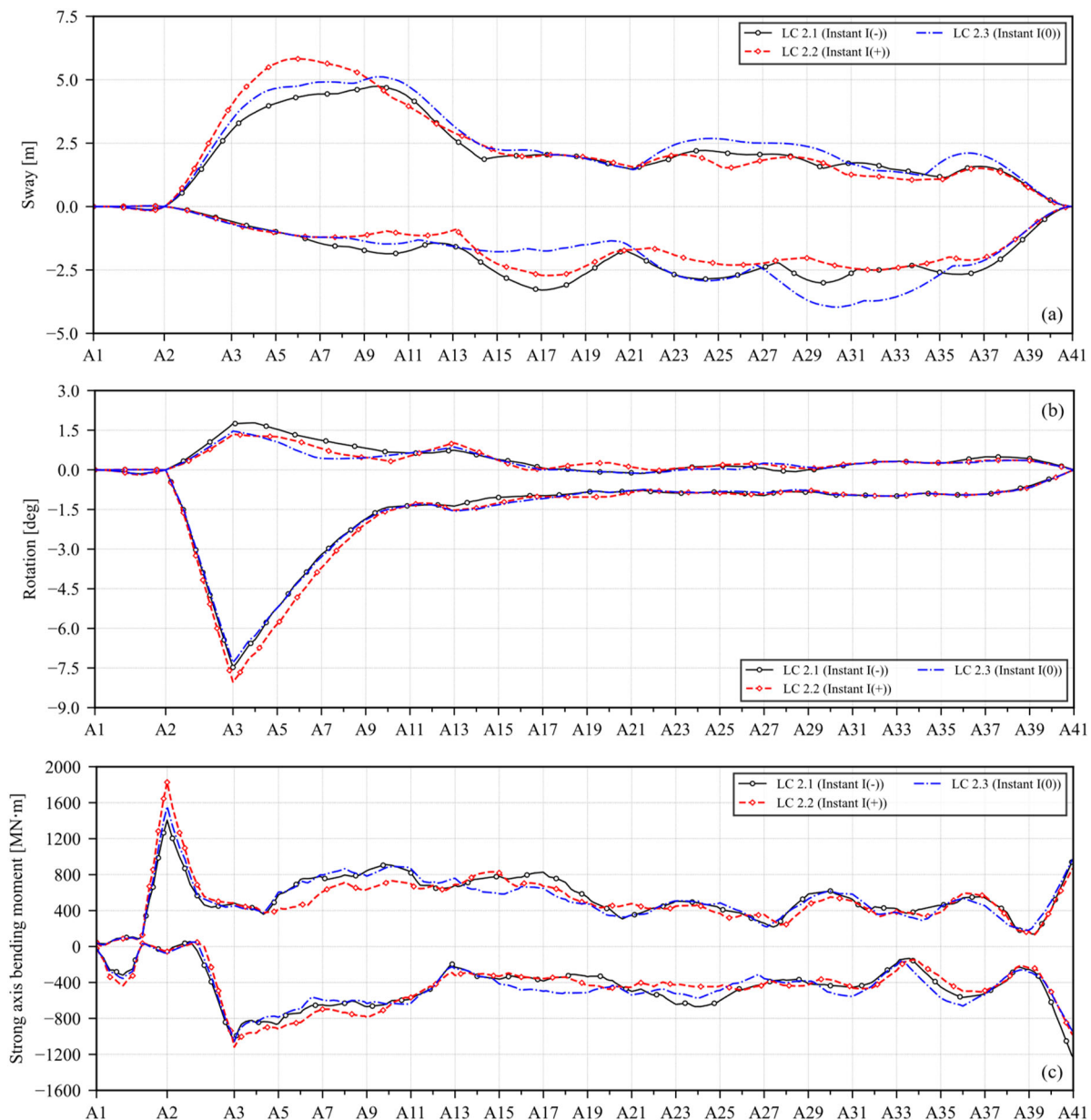

Figure 14. Maximum dynamic response of the bridge deck under multi-hazard load cases with different collision instants. (a) sway – horizontal displacement; (b) rotation about the longitudinal axis; (c) strong axis bending moment. (This figure is available in colour online.)

For the comfort and safety of bridge users, Eurocode (2002) recommends that the maximum allowable horizontal acceleration of any part of the bridge deck is 0.4 m/s^2, and the maximal acceleration in the vertical direction should not exceed 0.7 m/s^2 for crowd conditions. As shown in Figure 11(a), the horizontal accelerations in load cases with individual wind load and wave load are below the limiting value. The combined wind and wave load conditions yield exceeding acceleration at the vicinity of A3 and A36. The maximum acceleration reaches nearly 2.1 m/s^2 due to ship collision, as indicated in the pure ship collision load case. For the vertical accelerations presented in Figure 11(b), all the load cases except for the pure collision load case give excessive vertical accelerations, especially for the analysis under multi-hazard conditions. Another observation is that the cable-stayed part has relatively higher vertical accelerations because it is more sensitive to wind loads. Therefore, special considerations such as the
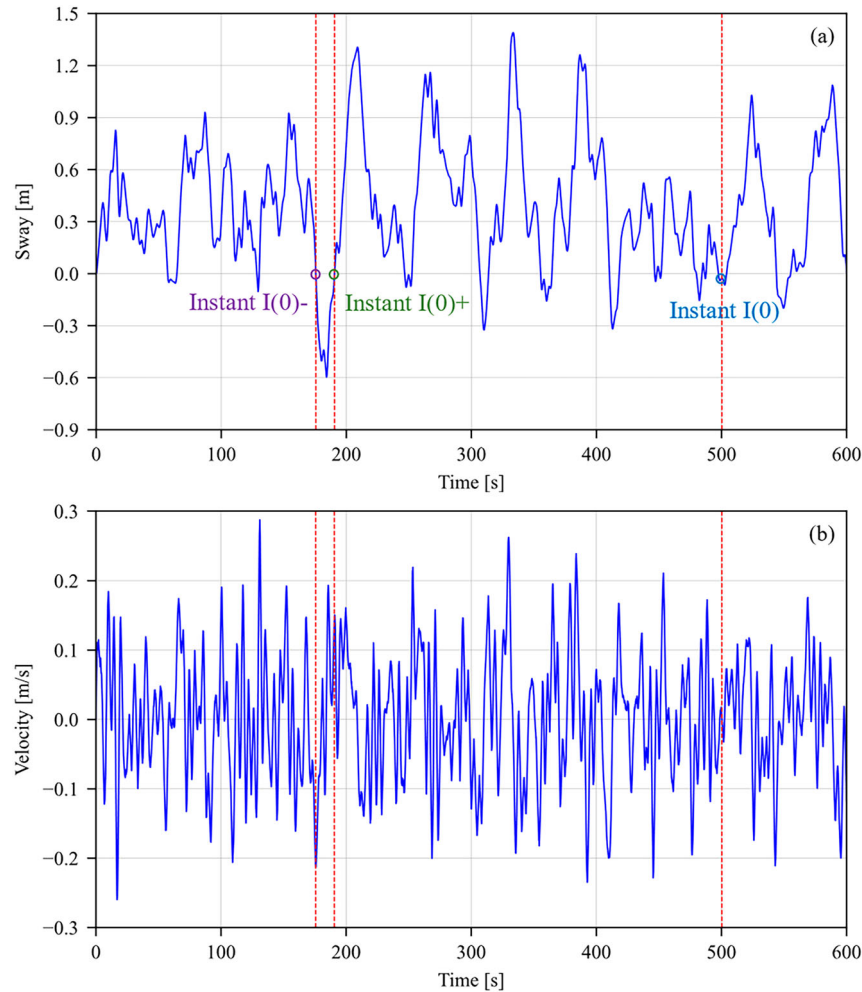

Figure 15. Three types of collision instants I(0) in the bridge deck response time histories at location A3 under combined wind and wave loads: (a) sway – horizontal displacement time history; (b) horizontal velocity time history. (This figure is available in colour online.)
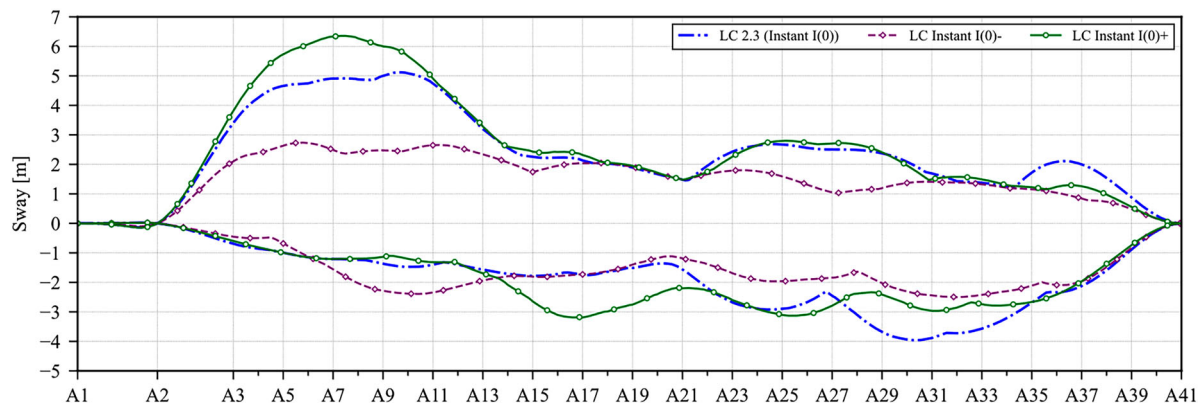

Figure 16. Maximum sway motion – horizontal displacement of the bridge deck under combined wind, wave and ship collision loads with collision instants I(0)+, I(0)- and I(0). (This figure is available in colour online.)

application of a damper system should be addressed in the bridge design to limit the accelerations against multi-hazard events. However, from the time history plots for accelerations at bridge deck A3 under the individual ship collision load case shown in Figure 12, it can be observed that both horizontal and vertical accelerations quickly damped out in about fifteen seconds.

Ship collision induces large horizontal shear forces at the cable-stayed bridge part and the floating bridge part between A3 and A9,

as shown in Figure 13(a). The multi-hazard load case has a maximum shear force that is 24.5% more than that in the individual ship collision load case. The maximum bending moment about the bridge deck strong axis is plotted in Figure 13(b). The strong axis bending moment is much larger in the multi-hazard case at the bridge tower, which has a 24.4% higher value than the pure ship collision case. In the continuous floating spans, the multi-hazard load condition has a higher influence on the spans between A3 to
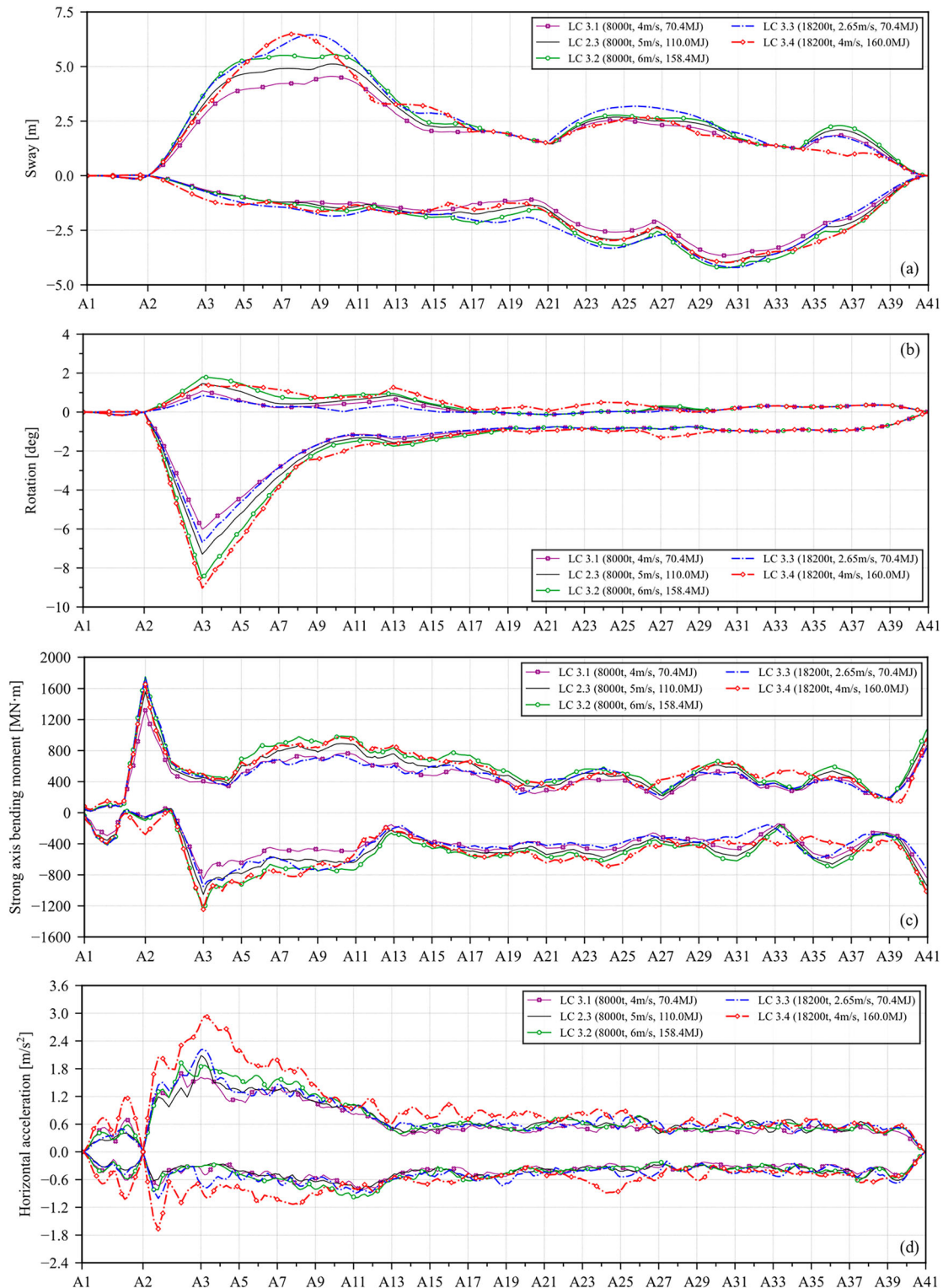

Figure 17. Maximum dynamic response of the bridge deck under multi-hazard load cases with different collision energies, ship masses, and collision velocities. (a) sway – horizontal displacement; (b) rotation about the longitudinal axis; (c) strong axis bending moment; (d) horizontal acceleration. (This figure is available in colour online.)

A13 and near the north end. There is a much smaller variation in the maximum strong axis bending moment in the rest of the floating spans away from the impact location. As can be observed, when ship collision is considered, the contributions from wind and wave loads become minor. As for the bending moment about the bridge weak axis, the absolute value of the maxima reaches the peak near A41, as shown in Figure 13(c). The maximum weak axis bending moment for the multi-hazard load case at A3 yields 25.2% larger value than the maximum weak axis moment induced by individual wind load.

5.2. Effects of different ship collision scenarios

After the comparison of the bridge behaviour between single-hazard and multi-hazard load cases, it is of interest to investigate how different collision scenarios affect the global bridge dynamic responses. The effects of collision instant, ship mass, collision

velocity, collision energy and collision location are further investigated under different multi-hazard conditions.

5.2.1. Collision instant

In LCs 2.1–2.3, the collision instant (starting time of ship-pontoon interaction) is varied among categories I(-), I(+) and I(0), while the collision energy is kept identical to 110 MJ. As presented in Figure 14(a), the maximum horizontal displacement of the bridge deck in LC 2.2 is 5.9 m, which is 15.7% and 25.5% larger than the maximum sway displacements in LCs 2.1 and 2.3, respectively. The discrepancy in the sway response is due to the different instantaneous pontoon positions resulting from combined wind and wave loads. Similar observations are obtained in the bridge deck rotation and strong axis bending moment, as shown in Figure 14(b,c). The cable-stayed bridge and the high floating bridge part experience higher rotation and strong axis
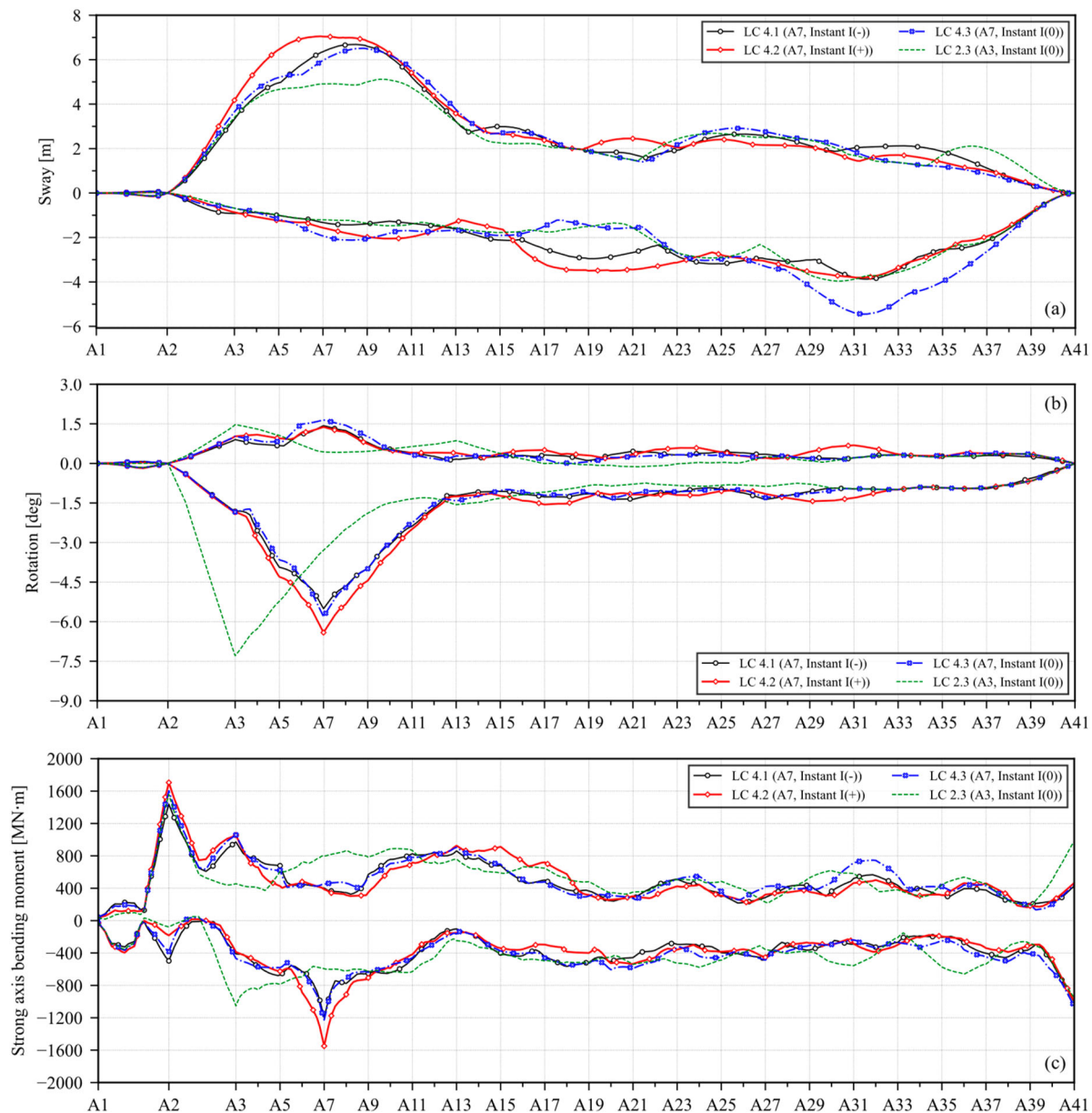

Figure 18. Maximum dynamic response of the bridge deck under multi-hazard load cases with different collision locations. (a) sway – horizontal displacement; (b) rotation about the longitudinal axis; (c) strong axis bending moment. (This figure is available in colour online.)

bending moment, while the variation in collision instant has negligible influence on the low floating bridge part.

Figure 15(a) shows the time history of the sway displacement at bridge deck A3 under wind and wave loads. Three types of collision instants I(0) with positive, negative and approximately zero horizontal velocities, labelled as I(0)+, I(0)- and I(0) respectively, are investigated. The horizontal velocities of the pontoon in the three cases are shown in Figure 15(b). In these three scenarios, ship collision occurs when the A3 pontoon is moving back to the static equilibrium position, with different instantaneous momentums. The comparisons of the maximum horizontal displacements induced by the combined wind, wave and ship collision loads with three different I(0) collision instants are illustrated in Figure 16. Even if the instantaneous pontoon position is almost identical for these three cases, the resultant maximum sway motion for collision instant I(0)+ is 24.2% larger than the LC 2.3 with collision instant I(0), while the analysis with collision instant I(0)- yields a 46.6% decrease in the maximum sway displacement. Therefore, the bridge response under combined wind, wave and ship collision loads is sensitive to both the instantaneous position and the instantaneous velocity of the struck pontoon.

5.2.2. Ship mass, striking velocity and collision energy

In LCs 3.1, 2.3, and 3.2, the 8000-t supply vessel strikes the A3 pontoon with an initial velocity of 4, 5, and 6 m/s, which represent a collision energy of 70.4, 110.0, and 158.4 MJ, accordingly. When the collision energy increases, the maximum horizontal displacement, angular rotation about the bridge longitudinal axis and strong axis bending moment increase, especially for the cable-stayed part and the floating part from A3 to A9 as shown in Figure 17(a–c).

The effect of different ship masses is investigated by comparing the results between LCs 3.1 and 3.4. A 18200-t container ship, which is one of the representative large ships travelling through the Bjørnafjord is selected (Statens Vegvesen 2019e). The striking velocity in LC 3.4 is identical to LC 3.1 with an increased collision energy of 160.0 MJ. A 41.4% higher maximum horizontal displacement value occurs at A7 in LC 3.4 than in LC 3.1. The angular rotation about the longitudinal bridge axis even has a difference of 50.0% between these two load cases.

However, as can be observed between LCs 3.1 and 3.3 from Figure 17(d), with a higher striking mass but a lower striking velocity, the horizontal acceleration experiences a higher peak even though the collision energy remains constant. Similar observations are obtained between LCs 3.2 and 3.4. The variation in container ship moving velocity and collision energy (LCs 3.3 and 3.4) tends to have limited effects on the maximum horizontal displacement and strong axis bending moment.

5.2.3. Collision location

To investigate the effect of ship collision location, two collision locations, i.e. A3 (LC 2.3) and A7 (LCs 4.1–4.3), are considered in this study. As shown in Figure 18(a), a collision at A7 with I(0) category (LC 4.3) causes a maximum horizontal displacement of 6.5 m at A9, which is about 32.7% larger than the value in the load case when the collision occurs at A3 (LC 2.3).

However, when the collision instant is altered to instant type I (+), the maximum sway displacement reaches its peak at A9 with a value of 7.1 m. This verifies the previous finding that the interactions among wind, wave and ship collision at different time instants highly affect the global behaviour of the floating bridge. As shown in Figure 18(b,c), a collision at A7 will lead to a slightly smaller maximum rotation but a considerably higher

value of the maximum strong axis bending moment in the high bridge part.

6. Conclusions

This study establishes a multi-hazard assessment framework for floating bridges under combined wind, wave and ship collision loads. A detailed numerical model of a curved floating bridge is developed in OrcaFlex. Time-domain simulation is conducted and the global dynamic response of the floating bridge under both single- and multi-hazard conditions has been investigated. The developed multi-hazard assessment method couples wind, wave and ship collision loads in one simulation, i.e. accounts for hazard interactions instead of a simple superposition of different load effects. The main conclusions of this study can be drawn as follows:

- The bridge motion in the vertical direction is primarily dominated by the wave loads. The combined wind and wave loads make large contributions to the horizontal responses of the entire floating bridge. Ship collision loads dominate the horizontal bridge deck motion, shear force and strong axis bending moment at the vicinity of the collision location for a relatively short period.
- Multi-hazard conditions yield considerably larger bridge responses than single-hazard conditions, in terms of deck displacements, rotations about the bridge longitudinal axis, accelerations, shear forces, and bending moments along the bridge deck. Therefore, multi-hazard assessment is vital in the design of floating bridges.
- The maximum bridge responses are sensitive to the collision instant to a great extent, due to the stochastic nature of wind and wave loads. The instantaneous pontoon position and velocity under combined wind and wave loads vary from time to time. Excessive horizontal displacement can occur when the struck pontoon moves to the furthest position away from the static equilibrium position followed by collision in the same direction, or the struck pontoon is moving with a large velocity along the collision direction.
- Higher striking velocity and collision energy induce dramatically larger bridge responses when the pontoon is collided by 8000-t supply vessels. However, they have minor influences under 18200-t container ship collisions in terms of maximum horizontal displacement and strong axis bending moment. With the same collision energy, increasing the ship mass with a relatively lower striking velocity causes a higher acceleration peak in the horizontal direction. Altering the ship mass and velocity also influences the interaction between the ship and the pontoon, thus affecting the local structural deformation and energy absorption.
- Ship collision location has a great effect on the bridge motion and the bridge deck internal forces and moments. When the collision location is changed from A3 to A7, much larger horizontal displacements and strong axis bending moments are obtained in the bridge deck. This implies the significance of considering different collision locations in the multi-hazard analyses.

There are several assumptions made in the bridge structure and load conditions modelling, which can be further improved in further development. Nevertheless, the main findings and conclusions presented are still representative of the problem at hand. The present study reveals the importance of multi-hazard assessment in the structural analysis of floating bridges. It is also essential to consider the interactions among different hazards. The proposed multi-hazard assessment framework can be used as a basis for a

more thorough evaluation of the bridge response under other hazards.

Disclosure statement

No potential conflict of interest was reported by the author(s).

Data availability statement

The data that support the findings of this study are available from the corresponding author upon reasonable request.

ORCID

Zihao Wang http://orcid.org/0000-0002-6174-4033
Yanyan Sha http://orcid.org/0000-0002-1880-1549
Jasna Bogunović Jakobsen http://orcid.org/0000-0001-9548-026X

References

Argyroudis SA, Mitoulis SA, Winter MG, Kaynia AM. 2019. Fragility of transport assets exposed to multiple hazards: state-of-the-art review toward infrastructural resilience. Reliab Eng Syst Saf. 191:106567. doi:10.1016/j.ress.2019.106567.

Banerjee S, Vishwanath BS, Devendiran DK. 2019. Multihazard resilience of highway bridges and bridge networks: a review. Struct Infrastruct Eng. 15(12):1694–1714. doi:10.1080/15732479.2019.1648526.

Bruneau M, Barbato M, Padgett JE, Zaghi AE, Mitrani-Reiser J, Li Y. 2017. State of the art of multihazard design. J Struct Eng. 143(10):03117002. doi:10.1061/(ASCE)ST.1943-541X.0001893.

Cheng Z, Gao Z, Moan T. 2018a. Dynamic response analysis of a floating bridge subjected to environmental loads. Proceedings of International Conference on Ocean, Offshore and Arctic Engineering, 17–22 June, Madrid, Spain. doi:10.1115/OMAE2018-77590.

Cheng Z, Gao Z, Moan T. 2018b. Hydrodynamic load modeling and analysis of a floating bridge in homogeneous wave conditions. Mar Struct. 59:122–141. doi:10.1016/j.marstruc.2018.01.007.

Cheynet E, Daniotti N, Jakobsen JB, Snæbjörnsson Jþ, Wang J. 2022. Unfrozen skewed turbulence for wind loading on structures. Appl Sci. 12(19):9537. doi:10.3390/app12199537.

Costa BMD, Wang J, Jakobsen JB, Øiseth OA, Snæbjörnsson Jþ. 2022. Bridge buffeting by skew winds: a quasi-steady case study. J Wind Eng Ind Aerodyn. 227:105068. doi:10.1016/j.jweia.2022.105068.

Cui M, Cheng Z, Moan T. 2022. A generic method for assessment of inhomogeneous wave load effects of very long floating bridges. Mar Struct. 83:103186. doi:10.1016/j.marstruc.2022.103186.

Cummins WE. 1962. The impulse response function and ship motions. Schiffstechnik. 47:101–109.

DNV. 2018. DNVGL-CG-0130: wave loads – rules and standards.

Eurocode. 2002. EN 1990: Eurocode – basis of structural design.

Eurocode. 2006. EN 1991-1-7: Eurocode 1 – actions on structures – part 1–7: general actions – accidental actions.

Eurocode. 2007. EN 1991-1-4: Eurocode 1 – action on structures – part 1–4: general actions – wind actions.

Fan W, Yuan W, Yang Z, Fan Q. 2011. Dynamic demand of bridge structure subjected to vessel impact using simplified interaction model. J Bridge Eng. 16(1):117–126. doi:10.1061/(ASCE)BE.1943-5592.0000139.

Fenerci A, Kvåle KA, Xiang X, Øiseth OA. 2022. Hydrodynamic interaction of floating bridge pontoons and its effect on the bridge dynamic responses. Mar Struct. 83:103174. doi:10.1016/j.marstruc.2022.103174.

Gholipour G, Zhang C, Mousavi AA. 2018. Effects of axial load on nonlinear response of RC columns subjected to lateral impact load: ship-pier collision. Eng Fail Anal. 91:397–418. doi:10.1016/j.engfailanal.2018.04.055.

Gill JC, Malamud BD. 2016. Hazard interactions and interaction networks (cascades) within multi-hazard methodologies. Earth Syst Dyn. 7(3):659–679. doi:10.5194/esd-7-659-2016.

IEC 61400-1. 2005. Wind turbines – part 1: design requirements. 3rd ed. Geneva: International Electrotechnical Commission.

Jin YL, Moan T, Sha Y. 2021. Numerical study of the structural consequences of ship impacts on a floating bridge in a risk analysis perspective. In: Amdahl J,

Soares CG, editors. Developments in the analysis and design of marine structures. London: CRC Press; p. 204–214.

Jonkman BJ, Kilcher L. 2012. Turbsim user's guide: version 1.06.00. Golden (CO): National Renewable Energy Laboratory.

Kvitrud A. 2011. Collisions between platforms and ships in Norway in the period 2001–2010. Proceedings of International Conference on Ocean, Offshore and Arctic Engineering, 19–24 June, Rotterdam, Netherlands. doi:10.1115/OMAE2011-49897.

Li Y, Ahuja A, Padgett JE. 2012. Review of methods to assess, design for, and mitigate multiple hazards. J Perform Constr Facil. 26(1):104–117. doi:10.1061/(ASCE)CF.1943-5509.0000279.

Mikkelsen O, Jakobsen JB. 2017. Aeroelastic response from indicial functions with a finite element model of a suspension bridge. IOP Conf Ser Mater Sci Eng. 276:012006. doi:10.1088/1757-899X/276/1/012006.

Moe OH, Sha Y, Veie J, Amdahl J. 2017. Analysis of tether anchored floating suspension bridge subjected to large ship collisions. Procedia Eng. 199:2488–2493. doi:10.1016/j.proeng.2017.09.413.

Oppong K, Saini D, Shafei B. 2020. Vulnerability assessment of bridge piers damaged in barge collision to subsequent hurricane events. J Bridge Eng. 25(8):04020051. doi:10.1061/(ASCE)BE.1943-5592.0001576.

Orcina. 2022a. OrcaFlex (Version 11.2c) documentation.

Orcina. 2022b. OrcaWave (Version 11.2c) documentation.

Rackwitz R, Flessler B. 1978. Structural reliability under combined random load sequences. Comput Struct. 9(5):489–494. doi:10.1016/0045-7949(78)90046-9.

Sha Y, Amdahl J. 2017. Ship collision analysis of a floating bridge in ferry-free E39 project. Proceedings of International Conference on Ocean, Offshore and Arctic Engineering, 25–30 June, Trondheim, Norway. doi:10.1115/OMAE2017-62720.

Sha Y, Amdahl J. 2019. Numerical investigations of a prestressed pontoon wall subjected to ship collision loads. Ocean Eng. 172:234–244. doi:10.1016/j.oceaneng.2018.11.054.

Sha Y, Amdahl J, Aalberg A, Yu Z. 2018. Numerical investigations of the dynamic response of a floating bridge under environmental loadings. Ships Offsh Struct. 13(sup1):113–126. doi:10.1080/17445302.2018.1426818.

Sha Y, Amdahl J, Dørum C. 2019. Local and global responses of a floating bridge under ship–girder collisions. J Offshore Mech Arct Eng. 141(3):031601. doi:10.1115/1.4041992.

Statens Vegvesen. 2015. Bruprosjektering – Håndbok N400. https://www.vegvesen.no/fag/publikasjoner/handboker/.

Statens Vegvesen. 2018. Document: MetOcean design basis. Document no.: SBJ-01-C4-SVV-01-BA-001. https://vegvesen.brage.unit.no/vegvesen-xmlui/handle/11250/2676915.

Statens Vegvesen. 2019a. Document: independent analyses of AMC floating bridge BJF 2019. Document no.: SBJ-32-C5-DNV-62-RE-023. https://vegvesen.brage.unit.no/vegvesen-xmlui/handle/11250/2670244.

Statens Vegvesen. 2019b. Document: preferred solution, K12 – Appendix A – drawings binder. Document no.: SBJ-33-C5-AMC-90-RE-101. https://vegvesen.brage.unit.no/vegvesen-xmlui/handle/11250/2660039.

Statens Vegvesen. 2019c. Document: preferred solution, K12 – Appendix F – global analyses – modelling and assumptions. Document no.: SBJ-33-C5-AMC-90-RE-106. https://vegvesen.brage.unit.no/vegvesen-xmlui/handle/11250/2660044.

Statens Vegvesen. 2019d. Document: preferred solution, K12 – Appendix G – global analyses – response. Document no.: SBJ-33-C5-AMC-90-RE-107. https://vegvesen.brage.unit.no/vegvesen-xmlui/handle/11250/2660075.

Statens Vegvesen. 2019e. Document: preferred solution, K12 – Appendix J – ship collision. Document no.: SBJ-33-C5-AMC-27-RE-110. https://vegvesen.brage.unit.no/vegvesen-xmlui/handle/11250/2660035.

Statens Vegvesen. 2019f. Document: preferred solution, K12 – Appendix K – design of floating bridge part. Document no.: SBJ-33-C5-AMC-22-RE-111. https://vegvesen.brage.unit.no/vegvesen-xmlui/handle/11250/2659987.

Statens Vegvesen. 2019g. Document: preferred solution, K12 – Appendix M – mooring system. Document no.: SBJ-33-C5-AMC-26-RE-113. https://vegvesen.brage.unit.no/vegvesen-xmlui/handle/11250/2659829.

Statens Vegvesen. 2019h. Document: preferred solution, K12 – Appendix R – risk assessment. Document no.: SBJ-33-C5-AMC-23-RE-118. https://vegvesen.brage.unit.no/vegvesen-xmlui/handle/11250/2660017.

Viuff T, Xiang X, Leira BJ, Øiseth OA. 2020. Software-to-software comparison of end-anchored floating bridge global analysis. J Bridge Eng. 25(5). doi:10.1061/(ASCE)BE.1943-5592.0001545.

Wang J, Cheynet E, Snæbjörnsson Jþ, Jakobsen JB. 2018. Coupled aerodynamic and hydrodynamic response of a long span bridge suspended from floating towers. J Wind Eng Ind Aerodyn. 177:19–31. doi:10.1016/j.jweia.2018.03.024.

Watanabe E. 2003. Floating bridges: past and present. Struct Eng Int. 13(2):128–132. doi:10.2749/101686603777964810.